The Taylor Interpolation through FFT Algorithm for Electromagnetic Wave Propagation and Scattering

Shaolin Liao[1]

[1]*Department of Electric and Computer Engineering, University of Wisconsin, Madison,*

1415 Engineering Drive, Madison, WI, USA, 53706

E-mail: sliao@wisc.edu

Abstract

The Taylor Interpolation through FFT (TI-FFT) algorithm for the computation of the electromagnetic wave propagation in the quasi-planar geometry within the half-space is proposed in this article. There are two types of TI-FFT algorithm, i.e., the spatial TI-FFT and the spectral TI-FFT. The former works in the spatial domain and the latter works in the spectral domain. It has been shown that the optimized computational complexity is the same for both types of TI-FFT algorithm, which is $\mathcal{N}_r^{\mathrm{opt}}\mathcal{N}_o^{\mathrm{opt}}\mathcal{O}(N\log_2 N)$ for an $N = \mathcal{N}_x \times \mathcal{N}_y$ computational grid, where $\mathcal{N}_r^{\mathrm{opt}}$ is the optimized number of slicing reference planes and $\mathcal{N}_o^{\mathrm{opt}}$ is the optimized order of Taylor series. Detailed analysis shows that $\mathcal{N}_o^{\mathrm{opt}}$ is closely related to the algorithm's computational accuracy γ_{TI}, which is given as $\mathcal{N}_o^{\mathrm{opt}} \sim -\ln\gamma_{\mathrm{TI}}$ and the optimized spatial slicing spacing between two adjacent spatial reference planes δ_z^{opt} only depends on the characteristic wavelength λ_c of the electromagnetic wave, which is given as $\delta_z^{\mathrm{opt}} \sim \frac{1}{17}\lambda_c$. The planar TI-FFT algorithm allows a large sampling spacing required by the sampling theorem. What's more, the algorithm is free of singularities and it works particularly well for the narrow-band beam and the quasi-planar geometry.

I. INTRODUCTION

The computation of electromagnetic wave propagation using the direct integration method is not efficient for the large-scale computation because the direct integration method has a daunting computational complexity of $\mathcal{O}\left(N^2\right)$ for an $N = \mathcal{N}_x \times \mathcal{N}_y$ computational grid, e.g., in the beam-shaping mirror system design for the Quasi-Optical (QO) gyrotron application, days of computation is required [1, 2, 3, 4, 5]. Fortunately, when the computational geometry is a plane, the FFT has been shown to be efficient in the electromagnetic wave computation [6, 7, 8], which has a computational complexity of $\mathcal{O}(N \log_2 N)$ and a low sampling rate only limited by the Nyquist rate. For the quasi-planar geometry, it will be shown in this article that the FFT can still be used with the help of the Taylor Interpolation (TI) technique.

The rest of this article is organized as follows. Section II gives the 2-Dimensional (2D) Fourier spectrum of the electromagnetic wave in its closed-form expression. Section III presents the optimized spatial and spectral types of TI-FFT algorithm. In Section IV, one numerical example is used to show the performance of the planar TI-FFT algorithm. Section V discusses the advantages and problems of the planar TI-FFT algorithm; some helpful suggestions are given. Finally, Section VI summarizes the planar TI-FFT algorithm. The scheme used to illustrate the planar TI-FFT algorithm is shown in Fig. 1 and the time dependence $e^{j\omega t}$ has been assumed in this article.

II. ELECTROMAGNETIC WAVE IN THE SPECTRAL DOMAIN

In this section, the 2D Fourier spectrum and far-field of the electromagnetic wave for the radiation integral are shown to be closely related to each other.

A. The radiation integral

For given electric and magnetic surface currents $(\mathbf{J}_s, \mathbf{J}_{ms})$, the radiating electric field $\mathbf{E}$ can be obtained under the Lorenz condition [9, 10], which is given as

$$\mathbf{E} = \frac{-j}{\omega\epsilon} \iint_S \left[k^2 \mathbf{J}_s(\mathbf{r}')G(\mathbf{R}) + \left(\mathbf{J}_s(\mathbf{r}') \cdot \nabla' \right) \nabla' G(\mathbf{R}) - j\omega\epsilon \mathbf{J}_{ms}(\mathbf{r}') \times \nabla' G(\mathbf{R}) \right] dV', \quad (1)$$
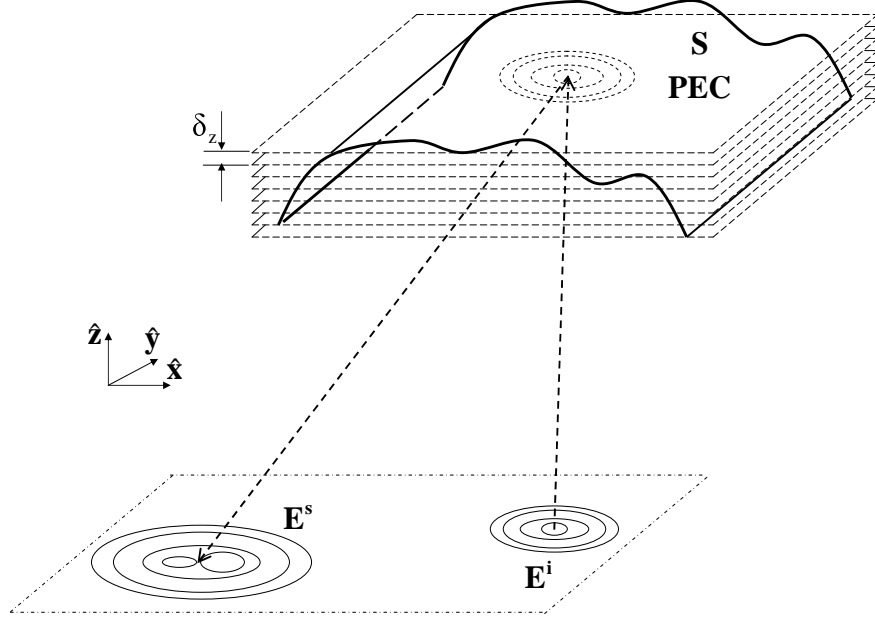
FIG. 1: Electromagnetic wave propagation and scattering: the computation of the electromagnetic wave propagation (the incident file $\mathbf{E}^i$) onto the PEC surface S is implemented through the spatial TI-FFT and the computation of the scattered electromagnetic field $\mathbf{E}^s$ from the PEC surface S is implemented through the spectral TI-FFTs and the inverse Fourier transform. δz is the spatial slicing spacing in the spatial TI-FFT.

where, ∇' is the gradient operator on the source coordinate $\mathbf{r}'$ and the scalar Green's function is given as

$$G(\mathbf{R}) = \frac{e^{-jk|\mathbf{R}|}}{4\pi|\mathbf{R}|}, \qquad \mathbf{R} \equiv \mathbf{r} - \mathbf{r}'. \tag{2}$$

B. The 2D Fourier spectrum of the scalar Green's function

Now apply the 2D Fourier transform on the scalar Green's function $G(\mathbf{R})$ in (2),

$$\mathcal{G}(k_x, k_y, \mathbf{r}') \equiv \mathrm{FT}_{2\mathrm{D}}\left[G(\mathbf{R})\right] = \frac{1}{2\pi}\int_{x=-\infty}^{\infty}\int_{y=-\infty}^{\infty}\frac{e^{-jk|\mathbf{R}|}}{4\pi|\mathbf{R}|}e^{jk_x x}e^{jk_y y}dxdy, \tag{3}$$

where k_z and the 2D Fourier transform has been defined as

$$k_z = \begin{cases} \sqrt{k^2 - k_x^2 - k_y^2}, & k_x^2 + k_y^2 < k^2 \\ -j\sqrt{k_x^2 + k_y^2 - k^2}, & k_x^2 + k_y^2 \geq k^2 \end{cases}, \tag{4}$$

3

$$\mathrm{FT}_{2\mathrm{D}}\left[\ \cdot\ \right] = \frac{1}{2\pi}\int_{x=-\infty}^{\infty}\left\{e^{jk_x x}\int_{y=-\infty}^{\infty}\left[\ \cdot\ \right]e^{jk_y y}dy\right\}dx, \tag{5}$$

From (3),

$$\mathcal{G}(k_x, k_y, \mathbf{r}') = \frac{1}{2\pi}e^{jk_x x'}e^{jk_y y'}\int_{x=-\infty}^{\infty}\left\{e^{jk_x(x-x')}\times\int_{y=-\infty}^{\infty}\left[\frac{e^{-jk|\mathbf{R}|}}{4\pi|\mathbf{R}|}e^{jk_y(y-y')}\right]dy\right\}dx, \tag{6}$$

Changing variables $u = x - x'$, $v = y - y'$ and $w = z - z'$, (6) becomes,

$$\mathrm{FT}_{2\mathrm{D}}\left[G(\mathbf{R})\right] = \frac{1}{2\pi}e^{jk_x x'}e^{jk_y y'}\int_{u=-\infty}^{\infty}\left\{e^{jk_x u}\times\int_{v=-\infty}^{\infty}\left[\frac{e^{-jk|\mathbf{R}|}}{4\pi|\mathbf{R}|}e^{jk_v v}\right]dv\right\}du \tag{7}$$

In the cylindrical coordinate,

$$|\mathbf{R}| = \sqrt{(r_\perp)^2 + w^2} \tag{8}$$

where $r_\perp = u^2 + v^2$ and the following relation can be obtained from (8),

$$dr_\perp = \frac{|\mathbf{R}|}{r_\perp}d|\mathbf{R}| \tag{9}$$

Now, express (7) in the cylindrical coordinate with the help of (9),

$$\mathcal{G}(k_x, k_y, \mathbf{r}') = \frac{1}{4\pi}e^{jk_x x'}e^{jk_y y'}\int_{|\mathbf{R}|=|w|}^{\infty}\left\{e^{-jk|\mathbf{R}|}\frac{1}{2\pi}\int_{\phi=0}^{2\pi}\left[e^{-jk_\perp r_\perp \cos(\psi-\phi)}\right]d\phi\right\}d|\mathbf{R}| \tag{10}$$

where $\psi = \arctan\left[\frac{k_y}{k_x}\right]$ and $\phi = \arctan\left[\frac{v}{u}\right]$. The integration over ϕ is the Bessel function of the first kind of order 0 and (10) reduces to

$$\begin{aligned}\mathcal{G}(k_x, k_y, \mathbf{r}') &= \frac{1}{4\pi}e^{jk_x x'}e^{jk_y y'}\int_{|\mathbf{R}|=|w|}^{\infty}\left[e^{-jk|\mathbf{R}|}\times J_0\left(k_\perp\sqrt{|\mathbf{R}|^2 - w^2}\right)\right]d|\mathbf{R}| \\ &= \frac{-j}{4\pi k_z}e^{jk_x x'}e^{jk_y y'}e^{-jk_z|z-z'|} \end{aligned} \tag{11}$$

Because only half-space $z > z'$ is of interest, only the 2D Fourier spectrum for half-space $z > z'$ will be considered in the rest of this article, which is obtained from (11) as

$$\mathcal{G}^>(k_x, k_y, \mathbf{r}') = \frac{-j}{4\pi k_z}e^{j\mathbf{k}\cdot\mathbf{r}'}e^{-jk_z z} \tag{12}$$

4

C. 2D Fourier spectra of Green's function related expressions

The 2D Fourier spectra of the derivatives (order n) of the scalar Green's function can be obtained from the property of the Fourier transform [7],

$$\frac{\partial^{(n)} G(\mathbf{R})}{\partial \tau^{(n)}} \implies (-jk_\tau)^n \mathcal{G}^>(k_x, k_y, \mathbf{r}'), \quad \tau = x, y, z. \tag{13}$$

Particularly, for the first-order and second-order derivatives,

$$\frac{\partial G(\mathbf{R})}{\partial \tau} \implies \frac{-k_\tau}{4\pi k_z} e^{j\mathbf{k}\cdot\mathbf{r}'} e^{-jk_z z}, \quad \tau = x, y, z. \tag{14}$$

$$\frac{\partial^2 G(\mathbf{R})}{\partial \tau^2} \implies \frac{jk_\tau^2}{4\pi k_z} e^{j\mathbf{k}\cdot\mathbf{r}'} e^{-jk_z z}, \quad \tau = x, y, z. \tag{15}$$

Similarly, the 2D Fourier spectra of the following expressions can be obtained for half-space $z > z'$,

$$\mathrm{FT}_{\mathrm{2D}}\left[\nabla G(\mathbf{R})\right] \implies -j\mathbf{k}\mathcal{G}^>(k_x, k_y, \mathbf{r}'). \tag{16}$$

$$\mathrm{FT}_{\mathrm{2D}}\left[\nabla^2 G(\mathbf{R})\right] \implies -k^2 \mathcal{G}^>(k_x, k_y, \mathbf{r}'). \tag{17}$$

$$\mathrm{FT}_{\mathrm{2D}}\left[\nabla\nabla G(\mathbf{R})\right] \implies -\mathbf{k}\mathbf{k}\mathcal{G}^>(k_x, k_y, \mathbf{r}'). \tag{18}$$

$$\mathrm{FT}_{\mathrm{2D}}\left[\overline{\overline{G}}_e(\mathbf{R})\right] \implies \mathcal{G}^>(k_x, k_y, \mathbf{r}')\left[\overline{\overline{I}} - \frac{\mathbf{k}\mathbf{k}}{k^2}\right]. \tag{19}$$

$$\mathrm{FT}_{\mathrm{2D}}\left[\overline{\overline{G}}_m(\mathbf{R})\right] \implies -j\mathcal{G}^>(k_x, k_y, \mathbf{r}')\left[\mathbf{k} \times \overline{\overline{I}}\right]. \tag{20}$$

where the dyadic Green's functions of the electric type ($\overline{\overline{G}}_e$) and the magnetic type ($\overline{\overline{G}}_m$) are given as

$$\overline{\overline{G}}_e(\mathbf{R}) = \left(\overline{\overline{I}} + \frac{1}{k^2}\nabla\nabla\right) G(\mathbf{R}). \tag{21}$$

$$\overline{\overline{G}}_m(\mathbf{R}) = \nabla G(\mathbf{R}) \times \overline{\overline{I}}. \tag{22}$$

D. The far-fields

In the far-field limit, $\mathbf{R} \simeq \mathbf{r} \to \infty$,

$$G(\mathbf{r}) = \frac{e^{-jk|\mathbf{r}|}}{4\pi|\mathbf{r}|}, \qquad \mathbf{R} = \mathbf{r} \text{ in the far-field limit.} \tag{23}$$

Similarly, the first-order derivative of the Green's function in the far-field limit can be obtained as

$$\frac{\partial G(\mathbf{r})}{\partial \tau} = \frac{\tau}{|\mathbf{r}|}\left(-jk - \frac{1}{|\mathbf{r}|^2}\right)\frac{e^{-jk|\mathbf{r}|}}{4\pi|\mathbf{r}|} \simeq -j\left(\frac{\tau}{|\mathbf{r}|}k\right)\frac{e^{-jk|\mathbf{r}|}}{4\pi|\mathbf{r}|} = -jk_\tau\frac{e^{-jk|\mathbf{r}|}}{4\pi|\mathbf{r}|}, \tau = x, y, z \tag{24}$$

where only $\frac{1}{|\mathbf{r}|}$ term is kept and the other terms ($\frac{1}{|\mathbf{r}|^2}, \frac{1}{|\mathbf{r}|^3}, \cdots$) are ignored. In derivation of (24), the following relation has been used in the far-field limit,

$$\frac{k_\tau}{k} = \frac{\tau}{|\mathbf{r}|}, \qquad \tau = x, y, z. \tag{25}$$

Following the similar procedure given in (24), the far-fields of derivatives (order n) of the scalar Green's function are obtained as

$$\frac{\partial^{(n)} G(\mathbf{r})}{\partial \tau^{(n)}} = (-jk_\tau)^n \frac{e^{-jk|\mathbf{r}|}}{4\pi|\mathbf{r}|}, \qquad \tau = x, y, z. \tag{26}$$

It is not difficult to see that the far-fields and the 2D Fourier spectra are closely related to each other.

E. The 2D Fourier spectra of the 3D spatial convolutions

It is not difficult to see that, the radiation integral in (1) can be expressed as the sum of the 3D spatial convolutions of some source terms with the Green's function related expressions. For simplicity, let's consider the 3D spatial convolution of an arbitrary source term $\mathbf{s}$ with the scalar Green's function G,

$$\mathbf{s}(\mathbf{r}) \overset{3D}{\bigotimes} G(\mathbf{r}) = \oiint_S \mathbf{s}(\mathbf{r}')G(\mathbf{R}) \, dS', \tag{27}$$

Now, apply the 2D Fourier transform on (27) and express the scalar Green's function $G(\mathbf{R})$ in the spectral domain,

6

$$S(\mathbf{k_x}, \mathbf{k_y}) \equiv \mathrm{FT}_{2\mathrm{D}} \left[\mathbf{s(r)} \overset{\mathrm{3D}}{\bigotimes} \mathbf{G(r)} \right] \tag{28}$$

$$= \frac{1}{2\pi} \int_{x=-\infty}^{\infty} \int_{y=-\infty}^{\infty} \left\{ e^{jk_x x} e^{jk_y y} \oiint_S \left[\mathbf{s(r')} \times \left(\frac{1}{2\pi} \int_{k_x'=-\infty}^{\infty} \int_{k_y'=-\infty}^{\infty} e^{-jk_x'(x-x')} e^{-jk_y'(y-y')} \right. \right. \right.$$

$$\left. \left. \left. \times \frac{-je^{-jk_z'(z-z')}}{4\pi k_z'} dk_x' dk_y' \right) \right] dS' \right\} dx dy,$$

First, do the integral over (x, y), (28) reduces to

$$S(\mathbf{k_x}, \mathbf{k_y}) = \oiint_S \left\{ \mathbf{s(r')} \int_{\mathbf{k_x'}=-\infty}^{\infty} \int_{\mathbf{k_y'}=-\infty}^{\infty} \left[e^{jk_x'x'} e^{jk_y'y'} \right. \right. \tag{29}$$

$$\left. \left. \times \frac{-je^{-jk_z'(z-z')}}{4\pi k_z'} \delta(k_x' - k_x) \delta(k_y' - k_y) dk_x' dk_y' \right] \right\} dS',$$

Next, do the integral over (k_x', k_y') and (29) reduces to

$$\mathrm{FT}_{2\mathrm{D}} \left[\mathbf{s(r)} \overset{\mathrm{3D}}{\bigotimes} G(\mathbf{r}) \right] = \mathbf{L} \left(\mathbf{s(r)} \right) \mathcal{G}^{>}(k_x, k_y, 0), \tag{30}$$

where $\mathbf{L}$ in (30) is the radiation vector [10] for source term $\mathbf{s}$, which is defined as

$$\mathbf{L} \left(\mathbf{s(r)} \right) = \iint_S \mathbf{s(r')} e^{j\mathbf{k} \cdot \mathbf{r'}} dS', \tag{31}$$

It is not difficult to see that the radiation vector $\mathbf{L}$ in (31) reduces to the regular 2D Fourier spectrum when surface S is a plane located at $z' = 0$.

$$\mathbf{L} \left(\mathbf{s(r)} \right) \bigg|_{z'=0} = 2\pi \mathrm{FT}_{2\mathrm{D}} \left[\mathbf{s}(x, y) \right], \tag{32}$$

where the dummy primed (x', y') have been replaced with (x, y). Substitute (31) into (30),

$$S(\mathbf{k_x}, \mathbf{k_y}) = \frac{-\mathbf{j}e^{-\mathbf{jk_z z}}}{4\pi \mathbf{k_z}} \mathbf{L}\left(\mathbf{s}(\mathbf{r})\right) = \mathcal{G}(\mathbf{k_x}, \mathbf{k_y}, \mathbf{0})\mathbf{L}\left(\mathbf{s}(\mathbf{r})\right). \tag{33}$$

It is not difficult to see that the radiation vector $\mathbf{L}$ in (31) is closely related to the far-field by letting $\mathbf{r} \rightarrow \infty$,

$$\mathbf{s}(\mathbf{r}) \overset{\text{3D}}{\bigotimes} G(\mathbf{r})\Big|_{\mathbf{r}\rightarrow\infty} = \frac{e^{-jk|\mathbf{r}|}}{4\pi|\mathbf{r}|}\mathbf{L}\left(\mathbf{s}(\mathbf{r})\right). \tag{34}$$

From (34), if $\frac{e^{-jk|\mathbf{r}|}}{4\pi|\mathbf{r}|}$ can be ignored, the radiation vector $\mathbf{L}$ can be considered as the far-field pattern, which means that when the far-field is obtained, the radiation vector and the 2D Fourier spectrum of the 3D convolution are also obtained, from (34) and (33) respectively.

F. 2D Fourier spectrum of the radiation integral

From (33) and (1), the 2D Fourier spectrum of the radiation integral (denoted as $\mathcal{F}$) is obtained, which is

$$\mathcal{F} = \frac{-\mathbf{j}}{\omega\epsilon}\mathcal{G}^{>}(\mathbf{k_x}, \mathbf{k_y}, \mathbf{0})\left\{\mathbf{k^2 L}\left(\mathbf{J}(\mathbf{r})\right) - \mathbf{k}\sum_{\tau=\mathbf{x,y,z}}\left[\mathbf{k_\tau L}\left(\mathbf{J_\tau}(\mathbf{r})\right)\right] + \omega\epsilon\mathbf{L}\left(\mathbf{J_m}(\mathbf{r})\right)\times\mathbf{k}\right\} \tag{35}$$

G. Electromagnetic field on a plane

After the 2D Fourier spectrum $\mathcal{F}$ has been obtained, the electric field $\mathbf{E}$ can be expressed in the PWS form [11, 12], which is given as,

$$\mathbf{E}(\mathbf{r}) = \text{IFT}_{\text{2D}}\left[\mathcal{F_0}(\mathbf{k_x}, \mathbf{k_y})e^{-\mathbf{jk_z z}}\right] \tag{36}$$

where $\mathcal{F_0}$ and the 2D Inverse Fourier Transform have been defined as

$$\mathcal{F_0}(\mathbf{k_x}, \mathbf{k_y}) = \mathcal{F_{0x}}\hat{\mathbf{x}} + \mathcal{F_{0y}}\hat{\mathbf{y}} + \mathcal{F_{0z}}\hat{\mathbf{z}} = \mathcal{F}(\mathbf{k_x}, \mathbf{k_y})e^{\mathbf{jk_z z}},$$

$$\mathcal{F}_{0z} = -\frac{k_x \mathcal{F}_{0x} + k_y \mathcal{F}_{0y}}{k_z},$$

$$\text{IFT}_{2\text{D}} \left[\ \cdot \ \right] = \frac{1}{2\pi} \int_{k_x=-\infty}^{\infty} \left\{ e^{-jk_x x} \int_{k_y=-\infty}^{\infty} \left[\ \cdot \ \right] e^{-jk_y y} dk_y \right\} dk_x.$$

III.   THE PLANAR TI-FFT ALGORITHM

In this section, the optimized spatial and spectral TI-FFTs are presented. It will be shown that both of them have the same computational complexity for the same quasi-planar surface.

A.   The spatial TI-FFT algorithm

It has been shown in (36) that the electric field $\mathbf{E}$ on a plane can be evaluated through the 2D inverse Fourier transform. For a quasi-planar surface, the TI technique can be used, which leads to the spatial TI-FFT algorithm (where the quasi-planar surface is sliced into many small spatial subdomains, as shown Fig. 1).

Rewrite the electric field $\mathbf{E}$ in (36) as follows,

$$\mathbf{E}(\mathbf{r}) = e^{-jkz}\text{IFT}_{2\text{D}} \left[\left[\tilde{\mathcal{F}}_0(\mathbf{k_x}, \mathbf{k_y}) \right] e^{j\triangle k_z \triangle z} \right], \quad \tilde{\mathcal{F}}_0(\mathbf{k_x}, \mathbf{k_y}) = \mathcal{F}_0(\mathbf{k_x}, \mathbf{k_y})e^{\mathbf{j}\triangle \mathbf{k_z}\mathbf{z}_{\min}} \quad (37)$$

where $z_{\min}$ denotes the minimum value of z. Now, express $e^{-j\triangle k_z \triangle z}$ into a Taylor series on the spatial reference plane located at $z = z_r$,

$$e^{j\triangle k_z \triangle z} = e^{j\triangle k_z \triangle z_r} \sum_{n=0}^{\mathcal{N}_o} \left[\frac{1}{n!} (j\triangle k_z)^n \left(z - z_r \right)^n \right], \quad (38)$$

where $\triangle z_r = z_r - z_{\min}$ and $\mathcal{N}_o$ is the order of Taylor series.

Substitute (38) into (37), the spatial TI-FFT algorithm for the electric field $\mathbf{E}$ is obtained,

$$\mathbf{E}(\mathbf{r}) = e^{-jkz} \sum_{n=0}^{\mathcal{N}_o} \left\{ \frac{1}{n!} \left[j\left(z - z_r \right) \right]^n \text{IFT}_{2\text{D}} \left[\tilde{\mathcal{F}}_0(\mathbf{k_x}, \mathbf{k_y})e^{\mathbf{j}\triangle \mathbf{k_z}\triangle \mathbf{z_r}} \left(\triangle \mathbf{k_z} \right)^{\mathbf{n}} \right] \right\}, \quad (39)$$

9

The number of spatial reference planes $\mathcal{N}_r$ required in the computation depends on the spatial slicing spacing $\left(\delta_z \equiv \max \left[z - z_r \right] = z_{r+1} - z_r \right)$ and the characteristic surface variation $\triangle z_c$ (within which the electromagnetic field is of interest): $\mathcal{N}_r \propto \triangle z_c / \delta_z$. The readers should note that the actual maximum interpolation distance is $\frac{\delta_z}{2}$, which is located at the middle of two adjacent spatial reference planes, but δ_z is used in this article to simplify the notation. Apparently, to achieve the desired computational accuracy (denoted as γ_{TI}), the choice of the spatial slicing spacing δ_z between two adjacent spatial reference planes depends on $\triangle k_{z,c}$, which is defined as

$$\triangle k_{z,c} \equiv k - k_{z,c} = k - \sqrt{k^2 - k_{\perp,c}^2} = k\alpha, \quad \alpha = 1 - \sqrt{1 - \left(\frac{k_{\perp,c}}{k} \right)^2}, \tag{40}$$

where, $k_{\perp,c}$ is the characteristic bandwidth (beyond which the 2D Fourier spectrum $\mathcal{F}$ is negligible) and is defined on x-y plane. It is clear that the smaller the bandwidth $k_{\perp,c}$, the larger the δ_z could be, which also means a smaller $\mathcal{N}_r$. So, a narrow-band beam and a small surface variation $\triangle z_c$ (quasi-planar geometry) are in favor of the planar TI-FFT algorithm.

In view of the importance of the spatial slicing spacing δ_z, it is helpful to define the characteristic wave length λ_c for a narrow-band beam. From (40),

$$\lambda_c \equiv \frac{2\pi}{\triangle k_{z,c}} = \frac{2\pi}{k - \sqrt{k^2 - k_{\perp,c}^2}} = \frac{\lambda}{\alpha}, \tag{41}$$

For a narrow-band beam $(k_{\perp,c} \ll k)$,

$$\lambda_c \sim 2 \left(\frac{k}{k_{\perp,c}} \right)^2 \lambda. \tag{42}$$

Fig. 2 plots the exact value in (41) and approximation in (42) of the characteristic wavelength λ_c for different characteristic bandwidth $k_{\perp,c}$, from which it can be seen that the maximum deviation of the approximation from the exact value is 1λ, which occurs at $k_{\perp,c} = k$.

It can be seen from (38) and (39) that, for the given computational accuracy γ_{TI}, the spatial slicing spacing δ_z should satisfy the following relation,

$$\gamma_{\mathrm{TI}} \sim \mathcal{O} \left[(\triangle k_{z,c} \, \delta_z)^{\mathcal{N}_o} \right] \tag{43}$$
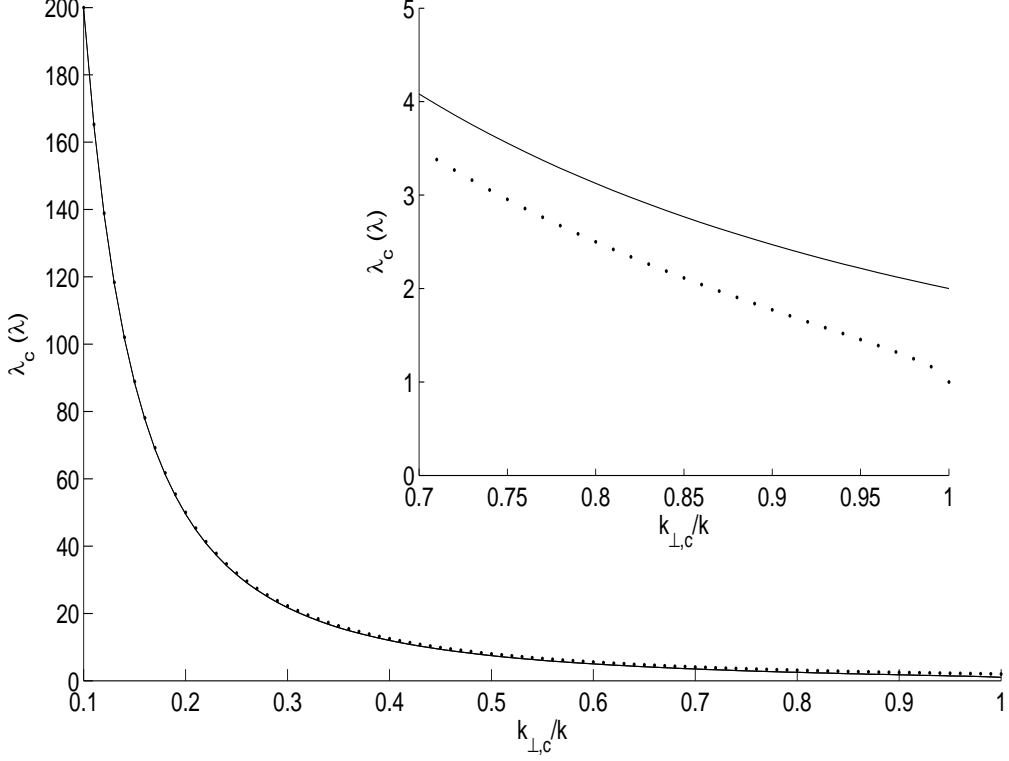
10

FIG. 2: The plots of the characteristic wavelength λ_c for different $k_{z,c}$. The exact value (line) is given in (41) and the approximation (dots) is given in (42). The plots show that $\lambda_c \gg \lambda$ for a narrow-band beam. The maximum deviation of the approximation from the exact value is 1λ, which occurs at $k_{z,c} = 0$ ($k_{\perp,c} = k$).

$$\rightarrow \delta_z \sim \frac{1}{k\alpha} \left(\frac{1}{\gamma_{\text{TI}}} \right)^{-\frac{1}{\mathcal{N}_o}} = \frac{\lambda}{2\pi\alpha} \left(\frac{1}{\gamma_{\text{TI}}} \right)^{-\frac{1}{\mathcal{N}_o}}, \tag{44}$$

For a narrow-band beam ($k_{\perp,c} \ll k$),

$$\delta_z \sim \frac{1}{\pi} \left(\frac{k}{k_{\perp,c}} \right)^2 \left(\frac{1}{\gamma_{\text{TI}}} \right)^{-\frac{1}{\mathcal{N}_o}} \lambda. \tag{45}$$

Now consider a quasi-planar surface with a characteristic surface variation of $\triangle z_c = \mathcal{N}_z \lambda$, from (44) the number of spatial reference planes $\mathcal{N}_r$ is given as

$$\mathcal{N}_r = \frac{\triangle z_c}{\delta_z} \sim 2\pi\alpha \left(\frac{1}{\gamma_{\text{TI}}} \right)^{\frac{1}{\mathcal{N}_o}} \mathcal{N}_z, \tag{46}$$

For a narrow-band beam ($k_{\perp,c} \ll k$),

11

$$\mathcal{N}_r \sim \pi \left(\frac{k_{\perp,c}}{k}\right)^2 \left(\frac{1}{\gamma_{\mathrm{TI}}}\right)^{\frac{1}{\mathcal{N}_o}} \mathcal{N}_z. \tag{47}$$

The number of FFT operations N_{FFT} and the computational complexity CPU are obtained as

$$N_{\mathrm{FFT}} = \mathcal{N}_o \times \mathcal{N}_r = 2\pi\alpha \left(\frac{1}{\gamma_{\mathrm{TI}}}\right)^{\frac{1}{\mathcal{N}_o}} \mathcal{N}_o \mathcal{N}_z, \tag{48}$$

$$\mathrm{CPU} = N_{\mathrm{FFT}} \; \mathcal{O}\left[N \log_2 N\right] = 2\pi\alpha \left(\frac{1}{\gamma_{\mathrm{TI}}}\right)^{\frac{1}{\mathcal{N}_o}} \mathcal{N}_o \mathcal{N}_z \; \mathcal{O}\left[N \log_2 N\right], \tag{49}$$

For a narrow-band beam $(k_{\perp,c} \ll k)$,

$$N_{\mathrm{FFT}} \sim \pi \left(\frac{k_{\perp,c}}{k}\right)^2 \left(\frac{1}{\gamma_{\mathrm{TI}}}\right)^{\frac{1}{\mathcal{N}_o}} \mathcal{N}_o \mathcal{N}_z. \tag{50}$$

$$\mathrm{CPU} \sim \pi \left(\frac{k_{\perp,c}}{k}\right)^2 \left(\frac{1}{\gamma_{\mathrm{TI}}}\right)^{\frac{1}{\mathcal{N}_o}} \mathcal{N}_o \mathcal{N}_z \; \mathcal{O}\left[N \log_2 N\right]. \tag{51}$$

For a narrow-band beam, the computational complexity CPU has a square law dependence on the characteristic bandwidth $k_{\perp,c}$ of the electromagnetic wave and have a linear dependence on the surface variation $(\triangle z_c = \mathcal{N}_z \lambda)$. The computational complexity CPU also has an inverse $\mathcal{N}_o{}^{\mathrm{th}}$-root dependence on the computational accuracy γ_{TI}. So the characteristic bandwidth $k_{\perp,c}$ has the most significant effect on the computational complexity of the planar TI-FFT algorithm.

It can be seen from (48) or (49) that the optimized number of Taylor series $\mathcal{N}_o^{\mathrm{opt}}$ can be obtained through finding the minimum value of N_{FFT} in (48) or CPU in (49) by assuming that $\mathcal{N}_o$ is a continuous variable,

$$\left.\frac{\partial N_{\mathrm{FFT}}}{\partial \mathcal{N}_o}\right|_{\mathcal{N}_o^{\mathrm{opt}}} = 0 \rightarrow \left.\frac{\partial \left[\ln\left[\mathcal{N}_o\right] - \ln\left[\gamma_{\mathrm{TI}}\right]\frac{1}{\mathcal{N}_o}\right]}{\partial \mathcal{N}_o}\right|_{\mathcal{N}_o^{\mathrm{opt}}} = 0, \tag{52}$$

$$\mathcal{N}_o^{\mathrm{opt}} \sim \mathrm{round}\left[\ln\left[\frac{1}{\gamma_{\mathrm{TI}}}\right]\right] = \mathrm{round}\left[-0.1151\gamma_{\mathrm{TI}}(\mathrm{dB})\right]. \tag{53}$$
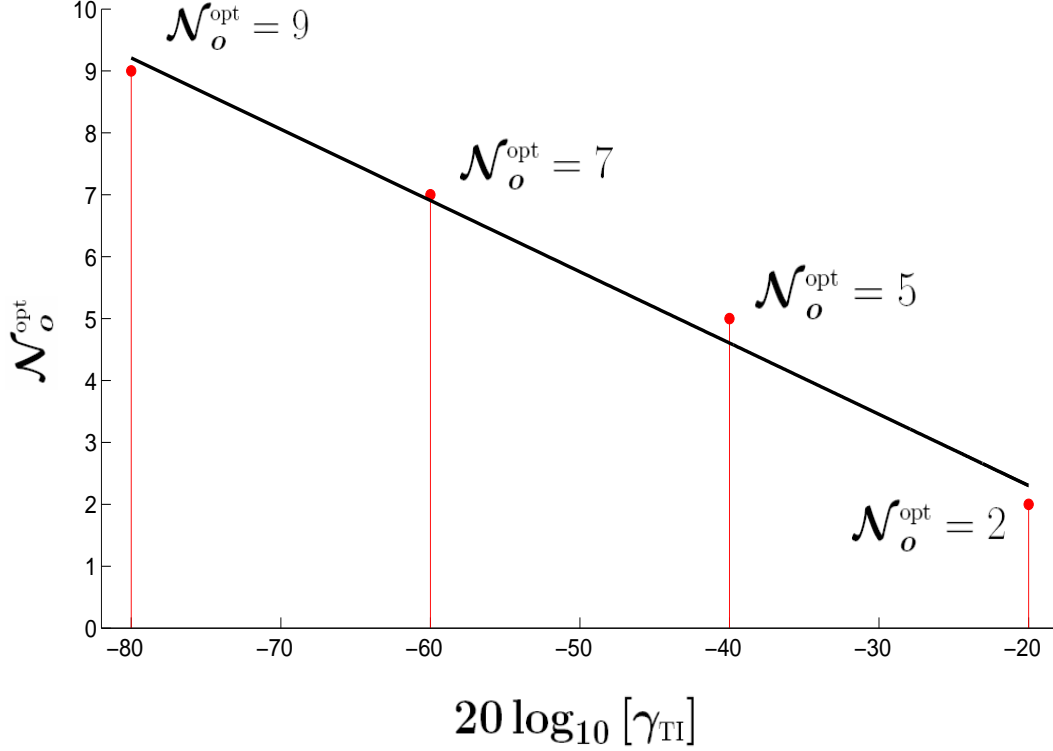
FIG. 3: The linear dependence of the optimized order of Taylor series $\mathcal{N}_o^{\mathrm{opt}}$ on the computational accuracy γ_{TI} (dB). It can be seen that $\mathcal{N}_o^{\mathrm{opt}} = (2, 5, 7, 9)$ for $\gamma_{\mathrm{TI}} = (-20, -40, -60, -80)$ dB respectively.

where "round" means to round the value to its nearest integer (actually, to achieve a higher computational accuracy γ_{TI}, the upper-bound could be used but the computational complexity CPU is a little higher). Fig. 3 also shows the linear dependence of the optimized order of Taylor series $\mathcal{N}_o^{\mathrm{opt}}$ on the computational accuracy γ_{TI} (dB), which has been shown in (53).

The optimized spatial slicing spacing δ_z^{opt} can be obtained from (44) and (53), which is

$$\delta_z^{\mathrm{opt}} \sim \frac{\lambda}{2\pi\alpha} \left(\frac{1}{\gamma_{\mathrm{TI}}} \right)^{-\frac{1}{\ln\left[\frac{1}{\gamma_{\mathrm{TI}}}\right]}} = \frac{\lambda}{2\pi e\alpha} \sim \frac{1}{17}\lambda_c, \tag{54}$$

For a narrow-band beam $(k_{\perp,c} \ll k)$,

$$\delta_z^{\mathrm{opt}} \sim \frac{1}{e\pi} \left(\frac{k}{k_{\perp,c}} \right)^2 \lambda, \tag{55}$$

where $e \sim 2.718$ is the natural logarithmic base. It is interesting to note that the optimized spatial slicing spacing δ_z doesn't depend on the computational accuracy γ_{TI} and strongly
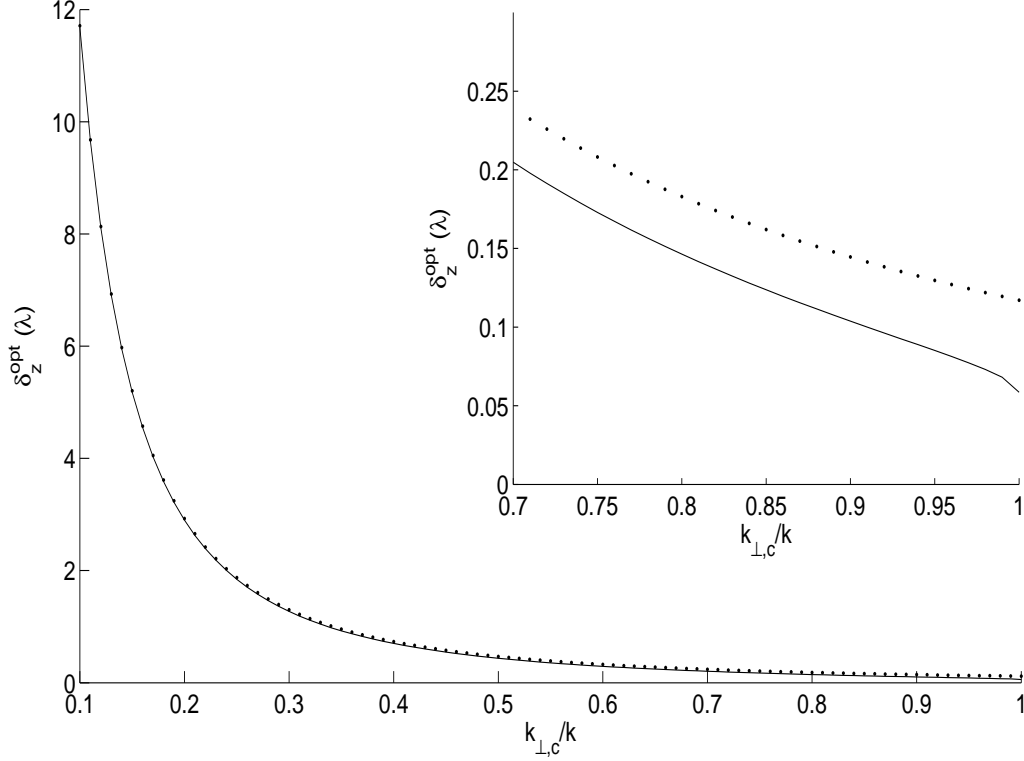
FIG. 4: Plots of the exact value (line) of δ_z^{opt} given in (54) and approximation (dots) given in (55) for different characteristic bandwidth $k_{\perp,c}$.

depends on the characteristic bandwidth $k_{\perp,c}$ (inverse square law). Fig. 4 shows δ_z^{opt} for different characteristic bandwidth $k_{\perp,c}$, from which it can be seen that $\delta_z^{\mathrm{opt}} > 0.5\lambda$ for $k_{z,c} > 0.9k$ ($k_{\perp,c} < 0.436k$).

The optimized number of spatial reference planes $\mathcal{N}_r^{\mathrm{opt}}$ is given as

$$\mathcal{N}_r^{\mathrm{opt}} = \frac{\triangle z_c}{\delta_z} = 2\pi e\alpha \mathcal{N}_z \sim 17\alpha\mathcal{N}_z, \tag{56}$$

For a narrow-band beam ($k_{\perp,c} \ll k$),

$$\mathcal{N}_r^{\mathrm{opt}} \sim \pi e \left(\frac{k_{\perp,c}}{k}\right)^2 \mathcal{N}_z. \tag{57}$$

Substitute (53) into (48) and (49), the optimized number of FFT operations $N_{\mathrm{FFT}}^{\mathrm{opt}}$ and the optimized computational complexity $\mathrm{CPU}^{\mathrm{opt}}$ can also be obtained,

$$N_{\mathrm{FFT}}^{\mathrm{opt}} = 2\pi e\alpha \ln\left[\frac{1}{\gamma_{\mathrm{TI}}}\right]\mathcal{N}_z, \tag{58}$$

14

For a narrow-band beam $(k_{\perp,c} \ll k)$,

$$N_{\text{FFT}}^{\text{opt}} \sim \pi e \left(\frac{k_{\perp,c}}{k} \right)^2 \ln \left[\frac{1}{\gamma_{\text{TI}}} \right] \mathcal{N}_z. \tag{59}$$

The optimized computational complexity CPU^{opt} is given as

$$\text{CPU}^{\text{opt}} \sim N_{\text{FFT}}^{\text{opt}} \mathcal{O} \left[N \log_2 N \right]. \tag{60}$$

B. The spectral TI-FFT algorithm

It has been shown in (35) that the computation of the 2D Fourier spectrum $\mathcal{F}$ is equivalent to evaluate the radiation vector $\mathbf{L}$. For the quasi-planar geometry, the FFT can still be used with the help of the TI technique, which leads to the spectral TI-FFT algorithm (where the spherical spectral surface is sliced into many small spectral subdomains, as shown Fig. 5).

From (31), the radiation vector $\mathbf{L}$ can be rewritten as

$$\mathbf{L} \left(\mathbf{f}(\mathbf{r}) \right) = 2\pi e^{jk_z z_{\min}} \text{FT}_{\text{2D}} \left[\widetilde{\mathbf{f}}(\mathbf{r}) e^{jk_z \triangle z} \right], \tag{61}$$

where $\widetilde{\mathbf{f}}(\mathbf{r}) = \frac{\mathbf{s}(\mathbf{r})}{\hat{\mathbf{n}} \cdot \hat{\mathbf{z}}}$ and $\hat{\mathbf{n}}$ is the normal to surface S. Now the Taylor expansion of $\mathbf{L}$ in (61) over k_z is given as

$$\mathbf{L} \left(\mathbf{f}(\mathbf{r}) \right) = 2\pi e^{jk_z z_{\min}} \sum_{n=0}^{\mathcal{N}_o} \left\{ \frac{1}{n!} \left(j \left[k_z - k_{z,r} \right] \right)^n \text{FT}_{\text{2D}} \left[\widetilde{\mathbf{f}}(\mathbf{r}) \left(\triangle z \right)^n \right] \right\}, \tag{62}$$

where $k_{z,r}$ denotes the spectral reference plane. For the given computational accuracy γ_{TI}, the spectral slicing spacing $\left(\delta k_z \equiv \max \left[k_z - k_{z,r} \right] = k_{z,r+1} - k_{z,r} \right)$ should satisfy the following relation,

$$\gamma_{\text{TI}} \sim \mathcal{O} \left[\left(\delta_{k_z} \triangle z_c \right)^{\mathcal{N}_o} \right], \tag{63}$$

$$\rightarrow \delta_{k_z} \sim \frac{1}{\triangle z_c} \left(\frac{1}{\gamma_{\text{TI}}} \right)^{-\frac{1}{\mathcal{N}_o}} \sim \frac{1}{\mathcal{N}_z \lambda} \left(\frac{1}{\gamma_{\text{TI}}} \right)^{-\frac{1}{\mathcal{N}_o}}, \tag{64}$$
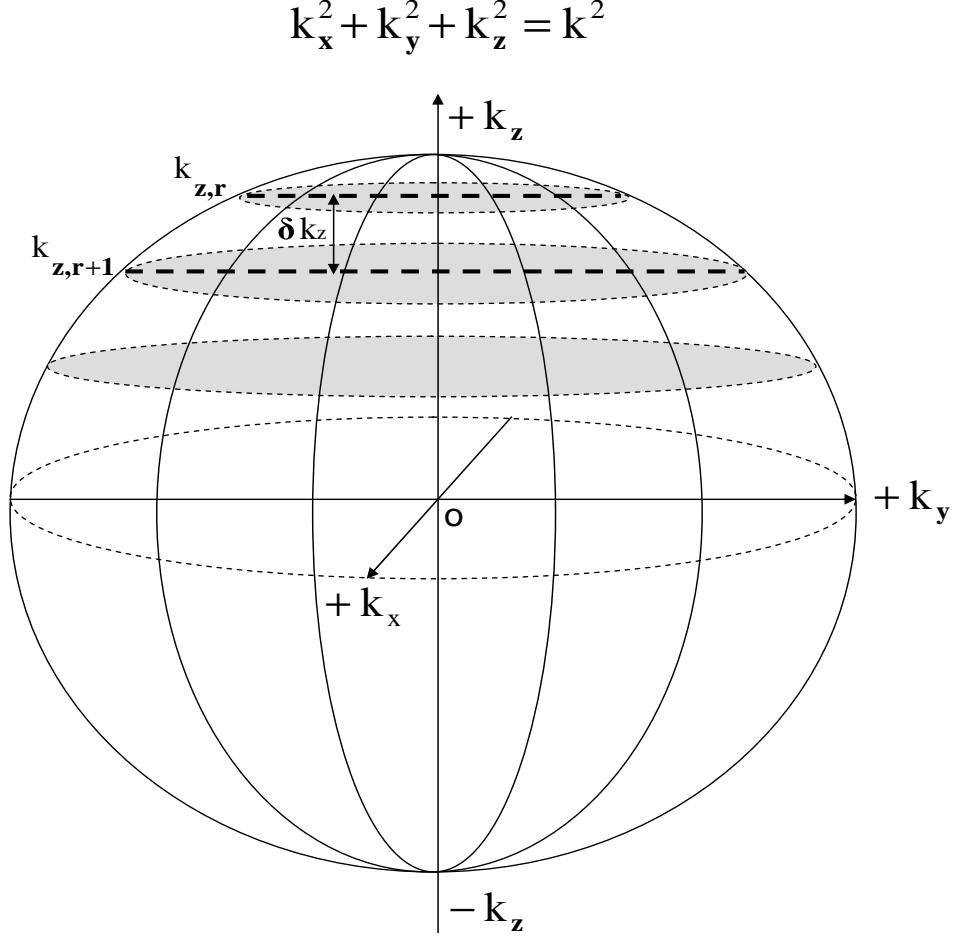
15

$$k_x^2 + k_y^2 + k_z^2 = k^2$$

FIG. 5: The spectral domain division for the *spectral* and TI-FFT: Only $k_z > 0$ half sphere surface is used for half-space $z > z'$ computation in this article. $k_{z,r}$ and $k_{z,r+1}$ denote the rth and $(r+1)^{\text{th}}$ spectral reference planes respectively. δ_{k_z} is the spectral slicing spacing.

The number of spectral reference planes $\mathcal{N}_r$ is given as

$$\mathcal{N}_r = \frac{\triangle k_{z,c}}{\delta_{k_z}} \sim 2\pi\alpha \left(\frac{1}{\gamma_{\text{TI}}} \right)^{\frac{1}{\mathcal{N}_o}} \mathcal{N}_z, \tag{65}$$

The number of FFT operations is given as

$$\mathcal{N}_{\text{FFT}} \sim 2\pi\alpha \left(\frac{1}{\gamma_{\text{TI}}} \right)^{\frac{1}{\mathcal{N}_o}} \mathcal{N}_o\mathcal{N}_z. \tag{66}$$

It is obvious that $\mathcal{N}_r$ in (65) and $\mathcal{N}_{\text{FFT}}$ in (66) are the same as those given in (46) and (48), which also means that the spatial and spectral TI-FFTs have the same optimized computational complexity.
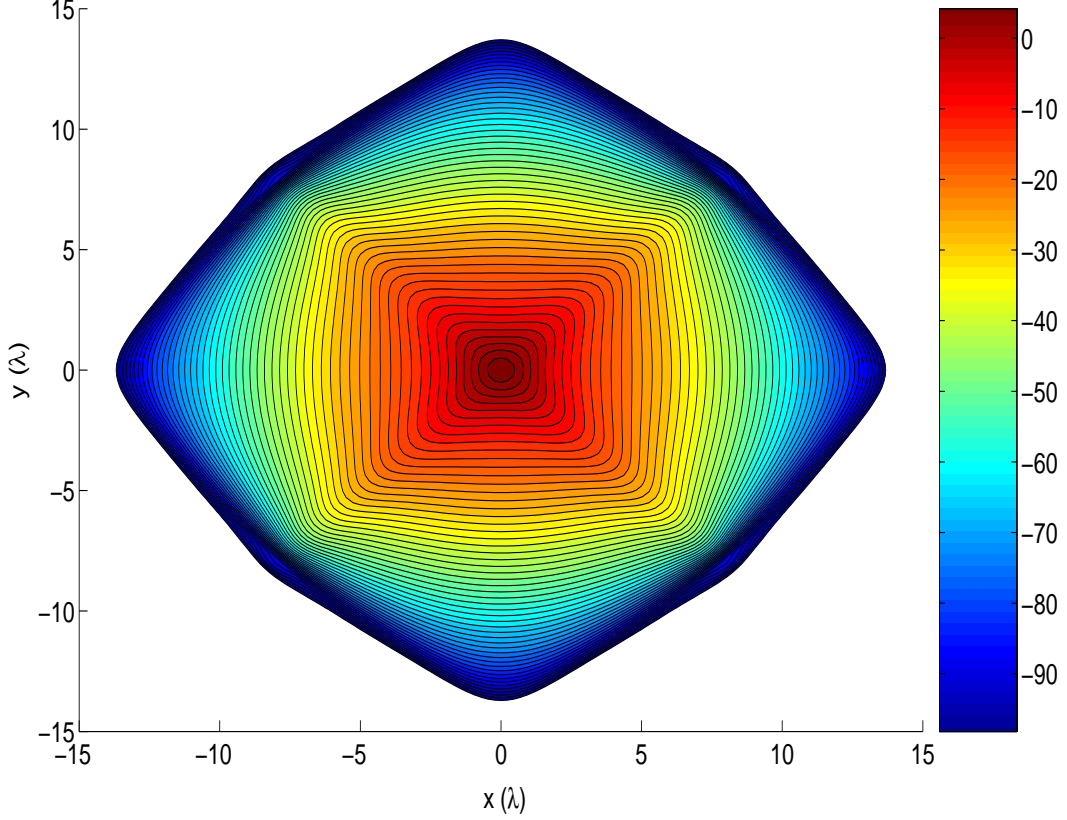
16

FIG. 6: The x-component (magnitude) of the scattered output field.

IV. COMPUTATIONAL RESULTS

To show the efficiency of the planar TI-FFT algorithm, the direct integration of the radiation integral in (1) has been used to make comparison with the planar TI-FFT algorithm. The numerical example used for such purpose is a 110 GHz Fundamental Gaussian Beam (FGB) scattered by a PEC quasi-planar surface with a sin wave perturbation. The 110 GHz FGB has a wavelength of $\lambda \sim 2.7$ mm.

A. The numerical results

The incident 110 GHz FGB propagates at $-\hat{\mathbf{z}}$ direction and has a beam waist radius of $w = 1$ cm. The quasi-planar PEC surface with a sine wave perturbation is described as

$$z(x,y) = -2.5\lambda + 0.5\lambda \cos\left(2\pi\frac{x}{15\lambda}\right)\cos\left(2\pi\frac{y}{15\lambda}\right). \tag{67}$$

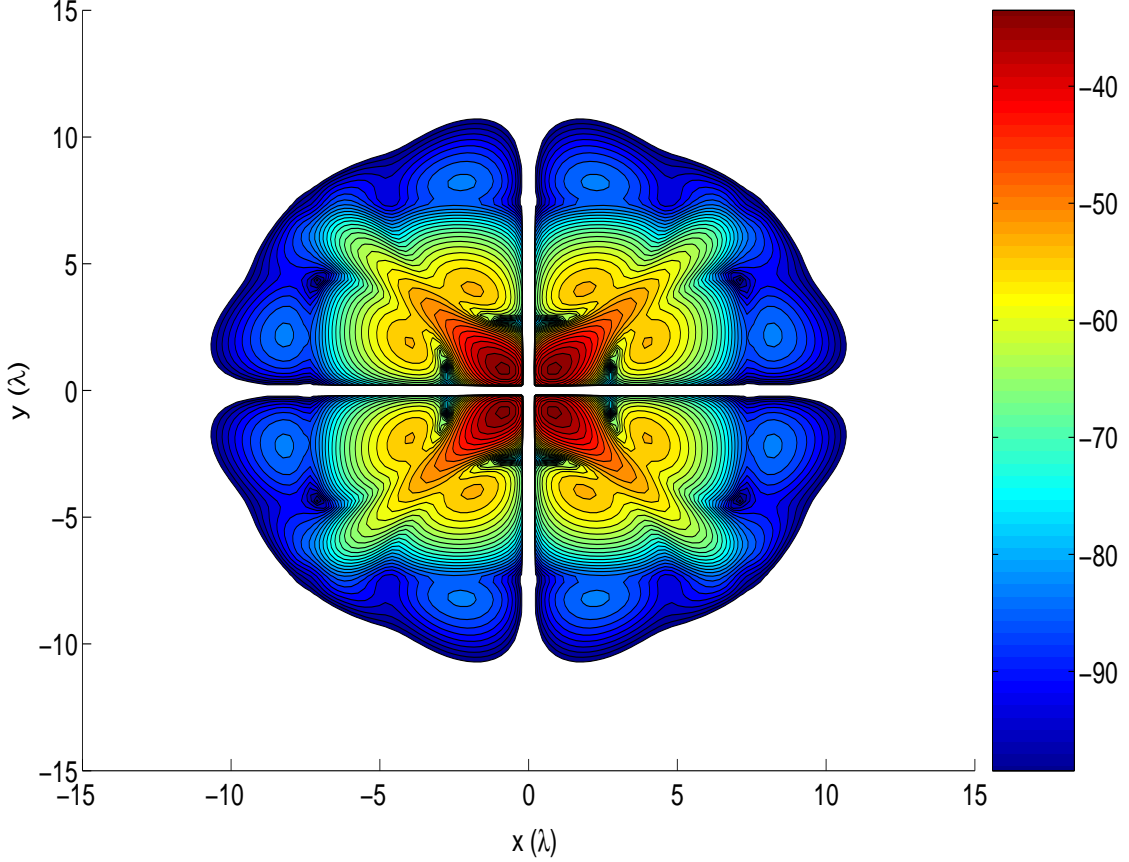In the numerical implementation of the planar TI-FFT algorithm, the computational

17

FIG. 7: The y-component (magnitude) of the scattered output field.

accuracy $\gamma_{\text{TI}} = 0.0001$ (-80 dB) has been used and the following optimized quantities are obtained from (53)-(60),

$$\mathcal{N}_o^{\text{opt}} \sim 9, \quad \delta_z^{\text{opt}} \sim 0.6\lambda, \quad \mathcal{N}_r^{\text{opt}} \sim \frac{1}{0.6} \sim 2, \quad N_{\text{FFT}}^{\text{opt}} \sim 18, \quad \text{CPU}^{\text{opt}} \sim 18\mathcal{O}\left[N\log_2 N\right] \text{ (68)}$$

where the quasi-planar surface described in (67) has a characteristic surface variation $\triangle z_c \sim 1\lambda$.

The scattered output field $\mathbf{E}^s$ are evaluated on plane $z = 0$ (where the incident 110 GHz FGB starts to propagate). Fig. 6, Fig. 7 and Fig. 8 show the magnitude patterns of x-, y-, and z-components of the scattered output field $\mathbf{E}^s$. The comparison of the result obtained from the planar TI-FFT algorithm and that from the direct integration method is given in Fig. 9, for both the magnitudes and the real parts, which shows that the planar TI-FFT algorithm has the desired -80 dB computational accuracy.
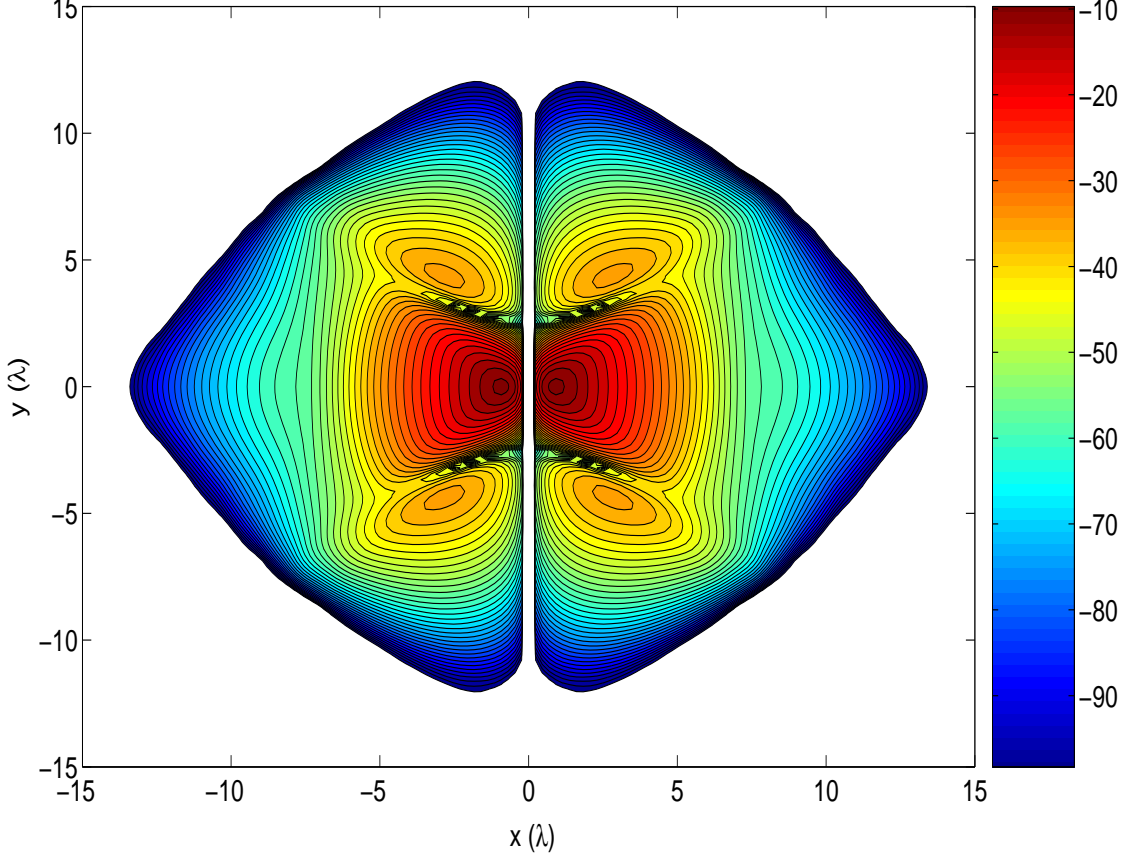
FIG. 8: The z-component (magnitude) of the scattered output field.

B. The CPU time and the accuracy

The CPU time t_{TI} for the planar TI-FFT algorithm and t_{DI} for the direct integration method have been summarized in Table I, together with the coupling coefficient defined as

$$\mathcal{C}_\tau \equiv \left| \frac{\iint \mathrm{E}^s_{\mathrm{TI},\tau}[\mathrm{E}^s_{\mathrm{DI},\tau}]^* \; dxdy}{\sqrt{\iint |\mathrm{E}^s_{\mathrm{TI},\tau}|^2 \; dxdy}\sqrt{\iint |\mathrm{E}^s_{\mathrm{DI},\tau}|^2 \; dxdy}} \right|_{z=0,} \tag{69}$$

where, $\mathrm{E}^s_{\mathrm{TI},\tau}$ and $\mathrm{E}^s_{\mathrm{DI},\tau}$ $(\tau = x, y, z)$ denote the scattered output field components obtained from the planar TI-FFT algorithm and the direct integration method respectively. From TABLE I, it can be seen that, even though at a large sampling spacing $\delta = 0.46\lambda$ $(\mathcal{N}_x = \mathcal{N}_y \sim 128)$, the coupling coefficients are still well above 90.00%. At this sampling rate, the direct integration method using Simpson's 1/3 rule is not accurate enough [1, 2, 3]. Also note that the coupling coefficients $\mathcal{C}_\tau$ $(\tau = x, y, z)$ reach their maximum values of 99.99% at $\mathcal{N}_x = \mathcal{N}_y \sim 256$ $(\delta_x = \delta_y = 0.23\lambda)$, after which the accuracies remain constant and thus the Nyquist rate can be estimated roughly as $\mathcal{N}_{\mathrm{Nyquist}} \sim 256$. The reason for this phenomenon
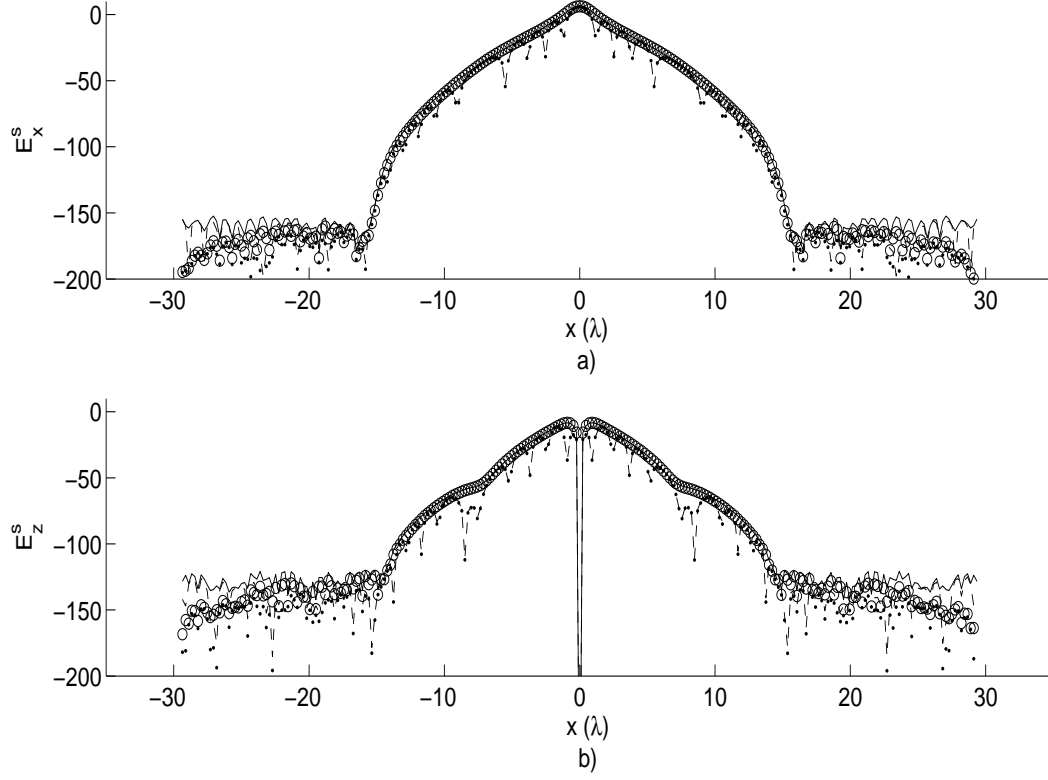
19

FIG. 9: The comparison of the scattered output field on plane $z = 0$, across the maximum value point of $|\mathrm{E}_x^s|$ and at $\hat{\mathbf{x}}$ direction: a) is for E_x^s; and b) is for E_z^s; solid lines (TI-FFT) and circles (direct integration method) are magnitudes; dashed lines (TI-FFT) and dots (direct integration method) are real parts.

is, that after the sampling rate increases above the Nyquist rate, further increasing the sampling rate will not give more information or computational accuracy.

The CPU time for the planar TI-FFT algorithm t_{TI} and for the direct integration method

TABLE I: CPU time (t_{TI}, t_{DI}) and coupling coefficient $\mathcal{C}_\tau$

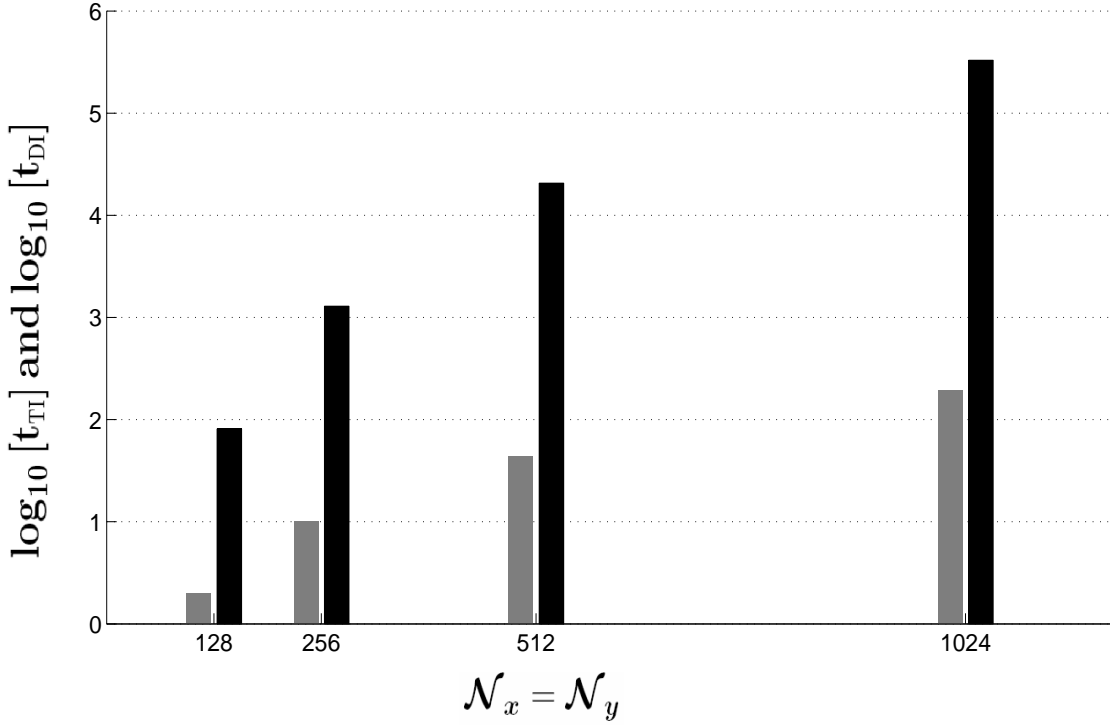| $\mathcal{N}_{x,y}$	$\delta(\lambda)$	t_{TI}(sec.)	t_{DI}(sec.)	$t_{\mathrm{DI}}/t_{\mathrm{TI}}$	$\mathcal{C}_x(\%)$	$\mathcal{C}_y(\%)$	$\mathcal{C}_z\ (\%)$
128	0.46	2	81	41	99.98	99.92	93.97
256	0.23	10	1289	129	99.99	99.99	99.99
512	0.12	44	20616	469	99.99	99.99	99.99
1024	0.06	194	329853	1700	99.99	99.99	99.99

20

FIG. 10: The CPU time (t_{TI}, t_{DI}) comparison: bars in gray color are for the planar TI-FFT algorithm and bars in black color are for the direct integration method. Note that the CPU time is in logarithmic scale (10-base).

t_{DI} are shown in Fig. 10. The ratio t_{DI}/t_{TI} is shown in Fig. 11.

All work was done in Matlab 7.0.1, on a 1.66 GHz PC (Intel Core Duo), with 512 MB Memory.

V. DISCUSSION: PROBLEMS AND POSSIBLE SOLUTIONS

Although the planar TI-FFT algorithm has so many advantages given above, some problems do exist in the practical applications.

1. Complicate geometry

As an example, consider surface S shown in Fig. 12, where the surface itself is not a quasi-planar surface and the direct implementation of the planar TI-FFT algorithm requires a large number of FFT operations, which can be seen from the spatial reference planes
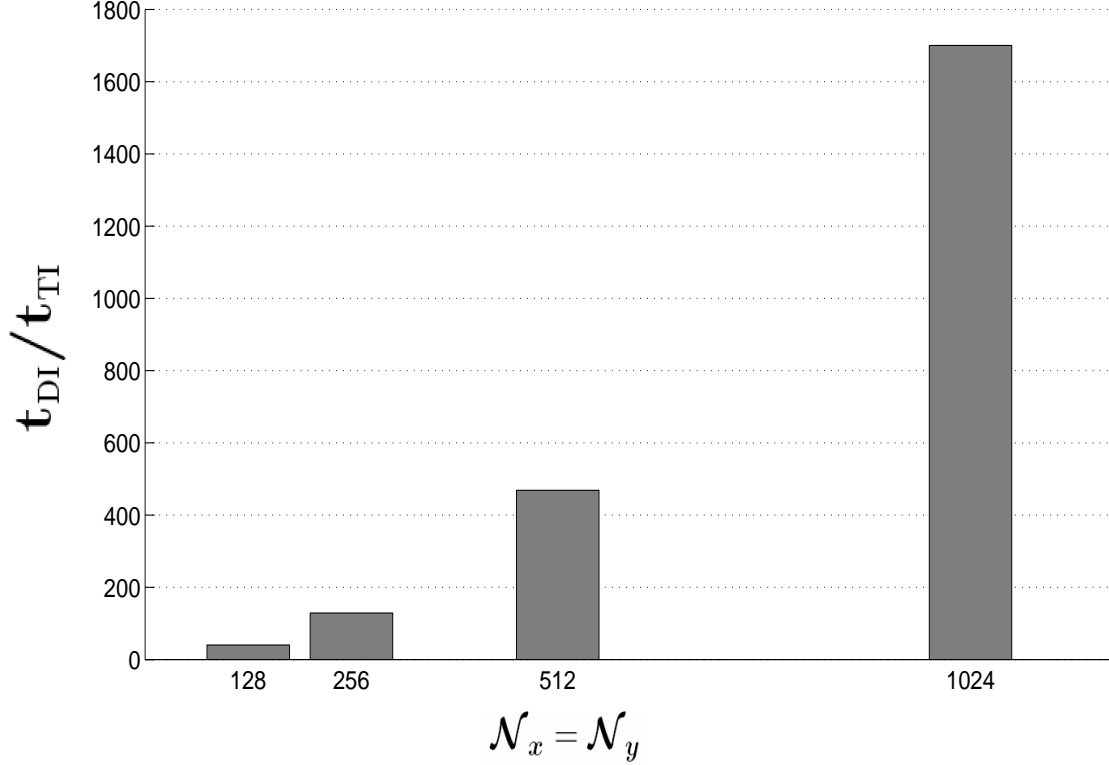
FIG. 11: The efficiency of the planar TI-FFT algorithm: the ratio of $t_{\mathrm{DI}}/t_{\mathrm{TI}}$ for $\mathcal{N}_x = \mathcal{N}_y = (128, 256, 512, 1024)$.

with a spatial slicing spacing δ_z. The problem can be solved by dividing surface S into two surface patches $\triangle S_1$ and $\triangle S_2$, which can be considered as quasi-planar surfaces and the planar TI-FFT can be used on them independently, with coordinate systems selected based on the spatial reference planes. At the extreme limit where surface patches $\triangle S_1$ and $\triangle S_2$ are planes, the number of FFT operations reduces to $\mathcal{N}_{\mathrm{FFT}} = 2$.

2. *Observation points not on the computational grid*

It is well-known that the FFT requires an even grid spacing (but δ_x and δ_y need not to be equal), which raises the question of how to calculate the electric field at points that are not exactly on the computational grid, e.g., the red filled circles in Fig. 13. One solution for this problem is to zero-pad the computational grid in the spectral domain, which corresponds to the interpolation of the computational grid in the spatial domain, as shown in Fig. 14. In the above example, it has been assumed that the observation points are evenly distributed
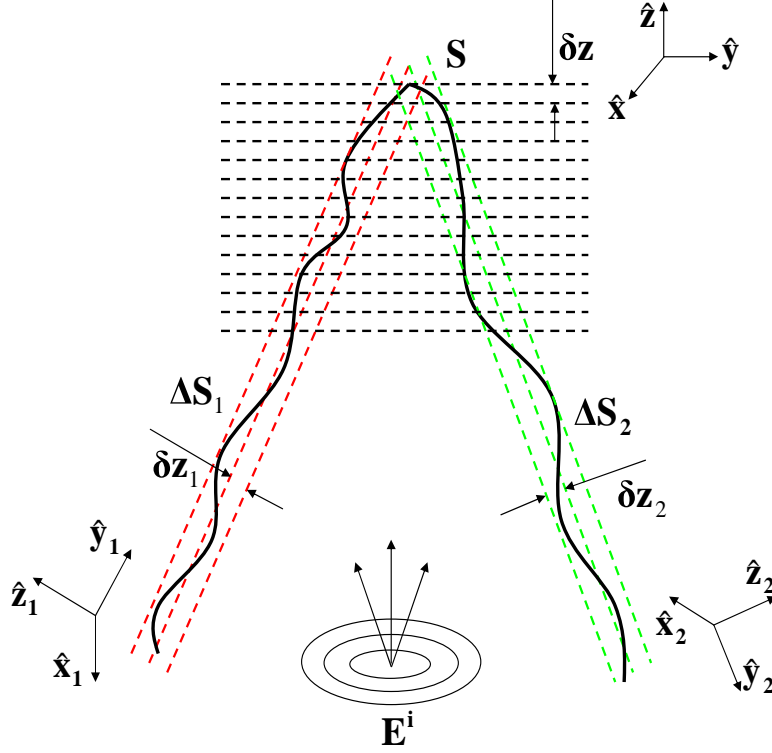
22

FIG. 12: An example of complicate surface S that can be divided into two quasi-planar surface patches $\triangle S_1$ and $\triangle S_2$. The computations of each surface patch is done in its corresponding coordinate system whose z-coordinate is perpendicular to the slicing spatial reference planes.

and the interpolation results are exact provided that the sampling rate is above the Nyquist rate [7]. For complicate observation point configurations (e.g., unevenly distributed points), the approximate techniques like the Gauss's forward/backward interpolations can be used.

3.   *The translation in spatial domain*

In the real situation, the source field surface and the observation surface are separate far away from each other (see Fig. 15). It is not practical nor necessary to use a large computational grid that covers both the source field surface and the observation surface. This kind of problem can be solved by using two computational grids, one for the source field surface and the other for the observation surface, with the same grid spacings (δ_x, δ_y). Then the translation of the observation coordinate system in the spatial domain, which is denoted as (x_0, y_0), corresponds to the phase shift in the spectral domain. Suppose the
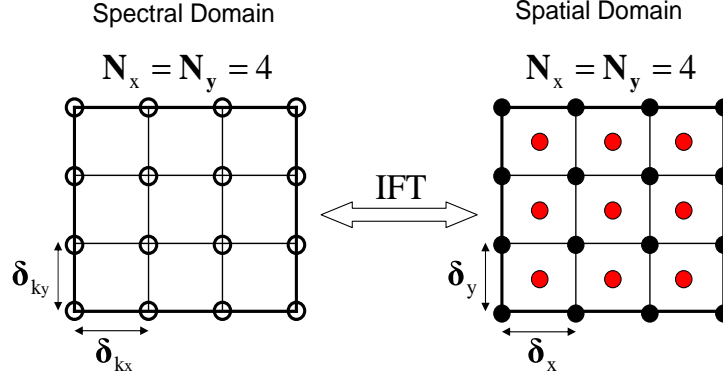
FIG. 13: The problem of computation of electromagnetic field on the observation points that are not on the computational grid (4×4), which are denoted as red filled circles in the spatial domain (assume that they are evenly distributed). $(\delta_{k_x}, \delta_{k_y})$ are grid spacings in the spectral domain. (δ_x, δ_y) are grid spacings in the space domain.
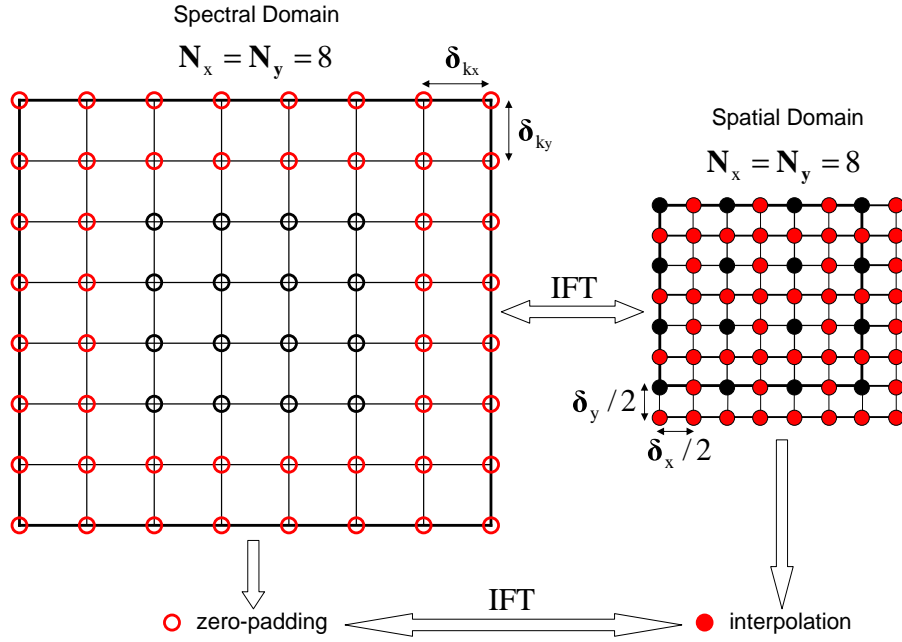

FIG. 14: The zero-padding in the spectral domain $(4 \times 4 \rightarrow 8 \times 8)$ corresponding to the interpolation in the spatial domain $(4 \times 4 \rightarrow 8 \times 8)$. $(\delta_{k_x}, \delta_{k_y})$ are still the same after zero-padding. But grid spacings in the spatial domain become $(\delta_x/2, \delta_y/2)$ after interpolation.

electric field in the source coordinate system is expressed as $\mathbf{E}(x' - x_0, y' - y_0)$, according to the property of the Fourier transform [7], the electric field $\mathbf{E}(x, y)$ in the observation coordinate system is given as
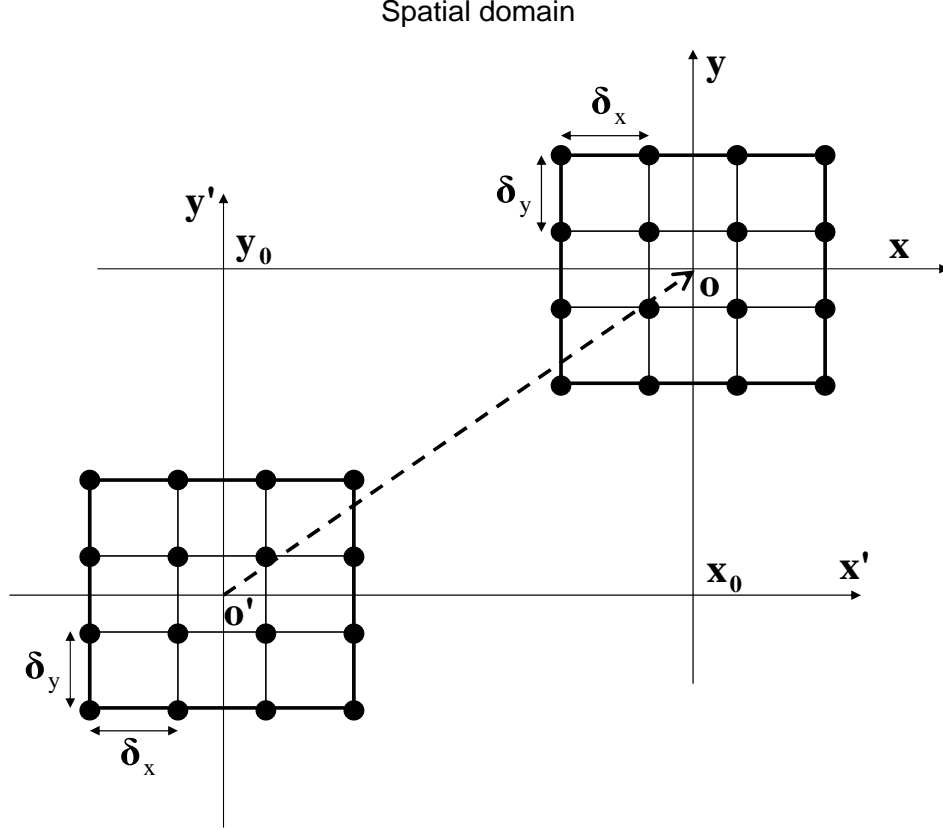
24

Spatial domain

FIG. 15: The translation of the source coordinate system $o'(0,0)$ to the observation coordinate system $o(x_0,\ y_0)$ in the spatial domain. Both the source and observation coordinate systems should have the same grid spacings $(\delta_x,\ \delta_y)$.

$$\mathbf{E}(x,y) = \mathrm{IFT}_{2\mathrm{D}}\left[e^{-jk_x x_0}e^{-jk_y y_0}\,\mathrm{FT}_{2\mathrm{D}}\left[\mathbf{E}(x'-x_0,y'-y_0)\right]\right]. \tag{70}$$

4. Computational redundancy

In the numerical implementation of the planar TI-FFT algorithm, the spatial domain or the spectral domain are divided into many small subdomains where the FFT can be used to interpolate the electromagnetic field (see Fig. 1 and Fig. 5). However, the FFT operation is done on the whole spatial or spectral domain even though the interpolation is only necessary on the relatively small subdomain, which causes the computational redundancy in the planar TI-FFT algorithm. Fortunately, the computational redundancy is small for a quasi-planar surface and a narrow-band beam.

VI.   CONCLUSION

In this article, the optimized planar TI-FFT algorithm for the computation of electro-magnetic wave propagation has been introduced for the narrow-band beam and the quasi-planar geometry. Two types of TI-FFT algorithm are available, i.e., the spatial TI-FFT and the spectral TI-FFT. The former is for computation of electromagnetic wave on the quasi-planar surface and the latter is for computation of the 2D Fourier spectrum of the electromagnetic wave. The optimized order of Taylor series used in the planar TI-FFT algorithm is found to be closely related to the algorithm's computational accuracy γ_{TI}, which is given as $\mathcal{N}_o^{\mathrm{opt}} \sim -\ln\gamma_{\mathrm{TI}}$ and the optimized spatial slicing spacing between two adjacent spatial reference planes only depends on the characteristic wavelength λ_c of the electro-magnetic wave, which is $\delta_z^{\mathrm{opt}} \sim \frac{1}{17}\lambda_c$. The optimized computational complexity is given as $\mathcal{N}_r^{\mathrm{opt}}\mathcal{N}_o^{\mathrm{opt}}\mathcal{O}\left(N\log_2 N\right)$ for an $N = \mathcal{N}_x \times \mathcal{N}_y$ computational grid. The planar TI-FFT algo-rithm allows a low sampling rate (large sampling spacing) required by the sampling theorem. Also, the algorithm doesn't have the problem of singularity. The planar TI-FFT algorithm has applications in near-field and far-field computations, beam-shaping mirror system de-signs, diffraction and scattering phenomena, millimeter wave propagation, and microwave imaging in the half-space scenario.

---

[1] Shaolin Liao and R. J. Vernon, "A new fast algorithm for field propagation between arbitrary smooth surfaces", In: *the joint 30th Infrared and Millimeter Waves and 13th International Conference on Terahertz Electronics*, Williamsburg, Virginia, USA, 2005, ISBN: 0-7803-9348-1, INSPEC number: 8788764, DOI: 10.1109/ICIMW.2005.1572687, Vol. 2, pp. 606-607.

[2] R. Cao and R. J. Vernon, "Improved performance of three-mirror beam-shaping systems and application to step-tunable converters", In: *the joint 30th Infrared and Millimeter Waves and 13th International Conference on Terahertz Electronics*, Williamsburg, Virginia, USA, 2005,

ISBN: 0-7803-9348-1, INSPEC number: 8788768, DOI: 10.1109/ICIMW.2005.1572692, Vol. 2, pp. 616-617.

[3] Michael P. Perkins and R. J. Vernon, "Iterative design of a cylinder-based beam-shaping mirror pair for use in a gyrotron internal quasi-optical mode converter", In: *the 29th Infrared and Millimeter Waves Conference*, Karlsruhe, Germany, Sep. 27-Oct. 1, 2004.

[4] Shaolin Liao and R. J. Vernon, "Sub-THz beam-shaping mirror designs for quasi-optical mode converter in high-power gyrotrons", *J. Electromagn. Waves and Appl.*, scheduled for volume 21, number 4, page 425-439, 2007.

[5] Shaolin Liao et. al., "On fast computation of electromagnetic wave propagation through FFT", *the 7th International Symposium on Antennas, Propagation, and EM Theory (ISAPE2006)*, Guilin, China, Oct. 26-Oct. 29, 2006.

[6] J. W. Cooley, J. W. Tukey, "An algorithm for the machine caculation of complex Fourier series", *Math. Comput.*, 19, 297301, 1965.

[7] A. V. Oppenheim, R. W. Schaffer, *Ditital Signal Processing*, Prentice-Hall, Englewood, Cliffs, NJ, 1975.

[8] Johnson J. H. Wang, "An examination of the theory and practices of planar near-field measurement", *IEEE Trans. on Antennas and Propagat.*, Vol. 36, No. 6, Jun., 1988.

[9] R. E. Collin, *Field Theory of Guided Waves*, second edition, IEEE press, 1991.

[10] C. A. Balanis, *Advanced Engineering Electromagnetic*, John Wiley & Son's Inc., 1989.

[11] G. T. Whittaker, G. N. Watson, *Mordern Analysis*, ch. XVIII, 4th ed., London: Cambridge Univ. Press, 1927.

[12] H. G. Booker, P. C. Clemmow, "The concept of an angular spectrum of a plane wave, and its relations to that of polar diagram and aperture distribution", *Proc. Inst. Elec. Engr.*, 97, 1950, pp. 11-17.